Nd$_{1.8}$Ce$_{0.2}$CuO$_{4+\delta}$:Ce$_{0.9}$Gd$_{0.1}$O$_{2-\delta}$ as a composite cathode for intermediate-temperature solid oxide fuel cells

A.P. Khandale, S.S. Bhoga[*]

Department of Physics, RTM Nagpur University, Amravati Road, Nagpur 440033, India

HIGHLIGHTS

- Composites prepared by impregnating Ce$_{0.9}$Gd$_{0.1}$O$_{2-\delta}$ in Nd$_{1.8}$Ce$_{0.2}$CuO$_{4\pm\delta}$ matrix.
- 20 vol.% Ce$_{0.9}$Gd$_{0.1}$O$_{2-\delta}$ dispersion resulted improved electrochemical performance.
- Impedance spectroscopy is useful to understand electrochemical processes.
- Impregnation of electrolyte may be a potential route to obtain composite cathode.

GRAPHICAL ABSTRACT
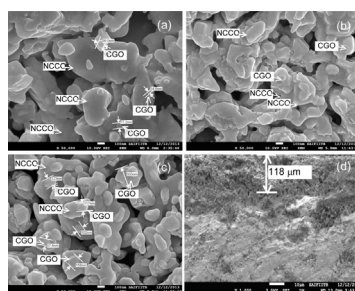
ARTICLE INFO

ABSTRACT

The $(100 - x)$Nd$_{1.8}$Ce$_{0.2}$CuO$_{4+\delta}$:(x)Ce$_{0.9}$Gd$_{0.1}$O$_{2-\delta}$ (x = 00, 10, 20 and 30 vol.%) composite systems are obtained by impregnating a stoichiometric solution of cerium and gadolinium nitrates followed by sintering at 900 °C for 4 h. Impregnating the Ce$_{0.9}$Gd$_{0.1}$O$_{2-\delta}$ not only inhibits the growth of the host Nd$_{1.8}$Ce$_{0.2}$CuO$_{4+\delta}$ grains during sintering but also enlarges the oxygen reduction reaction zone by introducing a nanosized phase that is ionically conductive, which significantly decreases the electrode polarization resistance of the composite cathode. A minimum polarization resistance value of 0.23 ± 0.02 Ω cm^2 is obtained at 700 °C for a (80)Nd$_{1.8}$Ce$_{0.2}$CuO$_{4+\delta}$:(20)Ce$_{0.9}$Gd$_{0.1}$O$_{2-\delta}$ composite cathode, and this value is attributed to the optimal dispersion into the porous Nd$_{1.8}$Ce$_{0.2}$CuO$_{4+\delta}$ matrix. The impedance spectra are modeled using an electrical equivalent model that consists of a mid-frequency Z_{R_1-CPE} circuit (parallel combination of R_1 and constant phase element (CPE)) and a low-frequency Gerischer impedance. The Gerischer impedance decreases significantly when Ce$_{0.9}$Gd$_{0.1}$O$_{2-\delta}$ infiltrates the Nd$_{1.8}$Ce$_{0.2}$CuO$_{4+\delta}$ matrix. The oxygen partial pressure-dependent polarization study suggests a medium-frequency response, which is due to charge transfer step; however, the low-frequency response corresponds to the non-charge transfer oxygen adsorption–desorption and the diffusion process during the overall oxygen reduction reaction process.

1. Introduction

Mixed ionic-electronic conductors (MIECs) with K$_2$NiF$_4$-type structures have received renewed interest due to their high electronic conductivity, adequate oxygen ion transport and strong electrocatalytic activity toward oxygen reduction reactions (ORR). Recently, research has focused on reducing the operating temperature of solid oxide fuel cells (SOFCs) by improving the electrode performance. The dispersion of nano-sized electrolyte particles extends the electrochemically active reaction zone, thus increasing the ORR kinetics of the electrode. In particular, impregnation has remained very effective when introducing/dispersing a nano-sized

* Corresponding author. Tel.: +91 9822366066; fax: +91 7122500736.
  E-mail address: msrl.physics1@gmail.com (S.S. Bhoga).

electrolyte phase into an electrode matrix [1]. Jiang et al. [2–4] reported improved performance for Ni-based anodes after impregnation with nano-sized yttria-stabilized zirconia (YSZ) or gadolinia-doped ceria (CGO). The 21.3 wt.% CGO-impregnated LaNi$_{0.6}$Fe$_{0.4}$O$_3$ cathode exhibited low polarization resistance (0.13 Ω cm^2) at 750 °C [5]. According to Wang et al. [6] impregnating porous samaria-doped ceria (SDC) with PrBaCo$_2$O$_{5+x}$ (PBC) nano-particles accelerated the oxygen ion incorporation and charge transfer steps compared to conventional PBC cathodes. Similarly, Huang et al. [7] also observed improved electronic conductivity and oxygen exchange reaction activity (decrease in the polarization resistance (0.18 Ω cm^2 at 700 °C)) for an Ag-infiltrated LaNi$_{0.6}$Fe$_{0.4}$O$_3$–SDC composite. During earlier investigations, Nd$_{1.8}$Ce$_{0.2}$CuO$_{4+\delta}$ (NCCO) was optimized to obtain the highest d.c. conductivity [8].

The electrical equivalent circuit model (ECM) is phenomeno-logical and easily accepted and understood; this model has been used extensively during SOFC performance diagnosis [9]. Idealized equivalent circuit models are often constructed to simulate the physical and chemical processes in SOFC systems. A cell structure with symmetrical electrodes is frequently constructed to isolate the contributions of the electrode toward the polarization losses from those of the electrolyte during SOFC performance [9].

Consequently, the present study aimed to improve the electro-chemical performance of NCCO further through impregnation with a CGO electrolyte. Each composition contained $(100 - x)$NCCO:(x) CGO $(x = 0 - 30)$ and was characterized using X-ray powder diffraction, scanning electron microscopy and d.c. conductivity. In addition, electrochemical impedance spectroscopy (EIS) studies on symmetric cells, which were constructed as cathode/CGO/cathode, were carried out relative to the temperature and oxygen partial pressure to determine the polarization resistance (R_p). The improved electrochemical properties can be understood based on the particle size, microstructure, electronic conductivity and percolation theory.

2. Experimental

Nd$_{1.8}$Ce$_{0.2}$CuO$_{4+\delta}$ was prepared through a combustion technique [10]. Cerium, neodymium and copper acetate (purity >99.9%, Aldrich Chemicals, USA) were used as reagents. All of the reagents, which were dried thoroughly, were combined in requisite stoi-chiometric ratio through dissolution in double distilled deionized water, separately. The prepared solutions were combined and stirred to obtain a homogeneous solution before being combusted using microwave oven at 800 W. The residue was ground and pressed (300 kN cm^{-2}) to obtain circular discs (pellets) 9 mm in diameter and 2 mm thick. The resultant pellets were sintered at 1000 °C for 4 h using high temperature electric furnace (Thermo-lyne, USA).

Stoichiometric amounts of cerium and gadolinium nitrate were dissolved in ethanol to obtain desired the x vol.% for the CGO in the composite. An appropriate amount of fine NCCO powder, which was prepared as discussed above, was added, and the solution was stirred for 3 h while using a magnetic stirrer. Diethylamine was added to precipitate the CGO in a NCCO matrix to obtain the $(100 - x)$NCCO:(x)CGO composites. Subsequently, the composite powder was dried at 80 °C for 12 h, pelletized (10 mm in diameter and 2 mm thick) and sintered at 900 °C for 4 h.

All of the sintered samples were characterized using X-ray powder diffraction, PANalytical X'pert PRO (Philips, The Netherlands) using CuKα radiation and a 1D pixel detector. The XRD measurements were carried out in a 2θ range from 10 to 100° with a step size and time per step of 0.025° and 1 s, respectively. The crystallite size of all studied materials was determined based on the diffraction peaks in a 2θ range of 30–50° while using the X'pert Highscore plus software
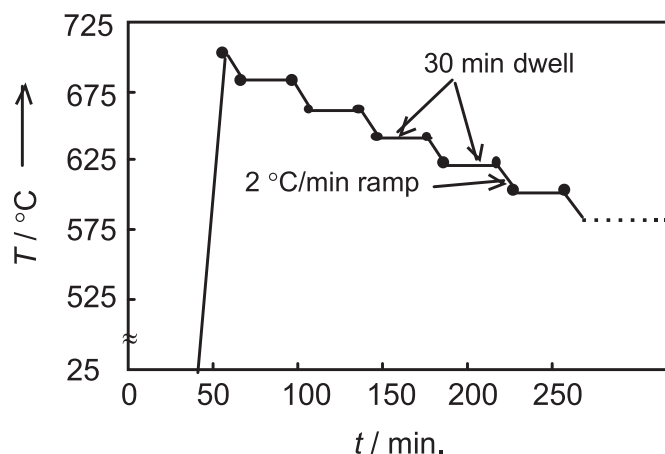

Fig. 1. Temperature profile during d.c. conductivity and EIS measurements.

with the Scherrer formula, as previously described [10]. The micro-structural and elemental analyses of a cathode composed of sym-metric cells were carried using field emission scanning electron microscopy (FESEM, Jeol JSM 7600-F, Germany) with EDS (Oxford, X-max 80 mm^2). The sintered densities of the samples were deter-mined using Archimedes' principle with a Mettler Toledo monopan balance and a density kit.

Before the d.c. conductivity measurements, the sintered sample, which was spring-loaded in a ceramic cell holder (Amel, Italy), was heated from 27 °C (room temperature) to 700 °C at 11 °C min^{-1}; this temperature was maintained for 30 min (dwell time) to homogenize the charge carriers. At the end of dwell time, the resistance was measured using a four-probe method with a computer-controlled Keithley 6221 current source and a 2182 A nanovoltmeter in delta mode. Later, the temperature of sample was decreased to 680 °C at 2 °C min^{-1}; after 30 min (dwell time), the resistance was measured as described above. This procedure was repeated during the cooling cycle (decrement of 20 °C in step) up to 500 °C. The temperature profile during the d.c. conductivity mea-surements is shown in Fig. 1. The temperature of the sample during the measurements was controlled within ±1 °C with a Eurotherm 2216e temperature controller.

The ink for each composite cathode was prepared by ball-milling (300 rotations per min (rpm) for 2 h) 1 g of the cathode powder, 3 wt.% polyvinyl buteral (binder), sodium free corn oil and ethyl-methyl ketone [8]. The particle size distribution of the cath-ode material in the ink/slurry was determined using a NanoPhox (Symphatec, Germany) particle size analyzer. The symmetric cells had the configurations given below and were prepared by spin coating the cathode ink on both flat surfaces of a sintered CGO pellet (96% relative density).

NCCO/CGO/NCCO	Cell-00
90NCCO:10CGO/CGO/90NCCO:10CGO	Cell-91
80NCCO:20CGO/CGO/80NCCO:20CGO	Cell-82
70NCCO:30CGO/CGO/70NCCO:30CGO	Cell-73

The EIS measurements for the symmetric cells were obtained using a computer-controlled Solartron 1255B FRA with a Solartron SI 1287 electrochemical interface versus the temperature (500–700 °C, during a cooling cycle, as depicted in Fig. 1), fre-quency (1×10^{-3}–1×10^6 Hz), and oxygen partial pressure (0.1–21 kPa), as described elsewhere [11]. The applied ac signal voltage was 5 mV.

3. Results and discussion

3.1. X-ray powder diffraction and energy dispersive X-ray spectroscopy

The X-ray powder diffraction (XRD) patterns of CGO, NCCO before sintering, NCCO after sintering, 90NCCO:10CGO, 80NCCO:20CGO and 70NCCO:30CGO are depicted in Fig. 2(a)–(f), respectively. All of the diffracted peaks are broader than usually observed for highly crystalline solids. The broadening in the diffracted peaks is attributed to the superfine crystalline nature of the NCCO and CGO. Before indexing, the XRD data were fitted with the X'pert Highscore plus software. The XRD patterns (Fig. 2(a) and (c)) of CGO and NCCO (after sintering) reveal that all of the characteristic diffracted peaks closely match the joint committee for powder diffraction standard (JCPDS) data file No. 01-075-0161 and file No. 01-079-1925 corresponding to cubic $Ce_{0.9}Gd_{0.1}O_{1.95}$ (CGO) and tetragonal $Nd_{1.8}Ce_{0.2}CuO_{4+\delta}$, respectively. In contrast, the few weak peaks attributed to NCCO in the background, which exhibited a very high level of noise (Fig. 2(b)), suggest that was NCCO exhibited little to no crystallinity before sintering. Therefore, crystalline NCCO in single phase cannot be generated by combustion alone. No peaks that corresponded to intermediate compounds are observed in the XRD patterns (Fig. 2(d)–(f)) for the composite cathodes. The relative intensities of the individual patterns for NCCO and CGO are generally proportional to the concentrations of these phases (Fig. 2(e) and (f)). The Rietveld method, which is usually preferred, is used with an external standard to estimate the relative vol.% of CGO in the composites. The volume fraction of CGO obtained from the XRD data and the actual/intended vol.% (taken during preparation of composites) for all of the compositions are compared in Table 1. Unless the concentration of CGO is low (10 vol.%), the actual and estimated vol.% of CGO are comparable. The large difference between the actual and estimated vol.% of CGO when $x = 10$ is attributed to the very large difference in the crystallite sizes

(Table 1) of NCCO (258 nm) and GDC (47 nm). Nevertheless, the CGO is dispersed in the requisite/intended vol.% in all composites.

The lattice cell constants (a and c) and crystallite sizes (C_s) of NCCO and CGO, which were determined from the XRD data are given in Table 1. Evidently, the lattice cell constants ($a \approx 0.394 \pm 0.004$ nm and $c \approx 1.207 \pm 0.003$ nm) corresponding to NCCO matched the JCPDS data closely ($a = 0.395$ nm and $c = 1.205$ nm, File No. 01-079-1925). Further, the lattice cell constant ($a \approx 0.54 \pm 0.004$) of CGO is close to the JCPDS value ($a = 0.5418$ nm; File No. 01-075-0161). The similarity of the lattice cell constants for the NCCO and CGO determined from XRD data (Table 1) suggests that either the Gd^{3+} from the CGO in the NCCO or the Nd^{3+}/Cu^{2+} from the NCCO in the CGO is insoluble. Table 1 reveals the steady decrease/increase in crystallite size of NCCO (from 273 to 193 nm)/CGO (from 47 to 146 nm) when increasing the CGO content in the composites. The decreasing NCCO crystallite size when increasing the CGO content is attributed to the presence of CGO nano-crystallites between the NCCO crystallites, inhibiting the growth of the NCCO crystallites during sintering. Leng et al. [12] reported that the ion conducting CGO in lanthanum strontium manganite (LSM) matrix inhibited the growth of the LSM grains during sintering. While sintering at high temperatures, however, the CGO nano-crystallites in the composites are grown at the cost of adjacent similar (CGO) crystallites through a well-known sintering process. The growth of CGO crystallites increases when the CGO content in the composites is increased, increasing the overall/average crystallite size of CGO (Table 1).

All of the studied compositions exhibit similar sintered densities (95–96%), as shown in Table 1. The theoretical and experimental values (obtained from the EDS of the selected grain (inset of Fig. 3)) for at.% $Nd_{1.8}Ce_{0.2}CuO_{4+\delta}$ (at electrode/electrolyte interface) given in Table 2 are closely matched. In addition, no characteristic emission peak(s) attributed to Gd were observed in the EDS spectrum (Fig. 3). Similarly, the characteristic emission peaks attributed to Nd and Cu were not observed in the EDS spectra of the CGO grain(s). Because the sample surface was coated with platinum (d.c. sputtering technique) for the SEM/EDS studies, the characteristic emission peaks attributed to platinum (Pt) appear in the EDS spectrum (Fig. 3). These results substantiate the XRD data (Table 1) discussed above. Therefore, the diffusion of neither Gd/Ce from CGO to NCCO nor Nd/Ce/Cu from NCCO to CGO occurred when sintering the composite at high temperatures. The NCCO and CGO exhibit excellent chemical stability relative to one another based on the XRD and EDS studies.

3.2. Scanning electron microscopy and particle size analysis

The scanning electron microphotographs (SEM) of the cleaved composite electrodes for Cell-91, Cell-82, Cell-73, and the fractured surface across the electrode/electrolyte interface of Cell-82 are depicted in Fig. 4(a)–(d), respectively. The morphologies of the NCCO (irregular shape) and CGO (spherical shape) particles (confirmed by EDS study) are distinguishable. The composite cathode consists of uniformly distributed nano-sized (34–100 nm) spherical CGO particles in the sintered NCCO matrix (Fig. 4(a)). The concentration and size (97–158 nm) of the CGO particles increase with an increase in its content (Fig. 4(b) and (c)) in composites. Both of these observations agree with the XRD results discussed in subsection 3.1. The uniform arrangement of the nano-grains generated a sufficient number of sub-micron-sized pores, which facilitate gas diffusion through cathode layer. The microphotograph of the electrode/electrolyte interface shown in Fig. 4(d) reveals a thin cathode layer (≈ 18 μm) with a porous morphology over a highly dense CGO electrolyte. In addition, the homogenous contact that formed along the interface between the electrode and electrolyte is
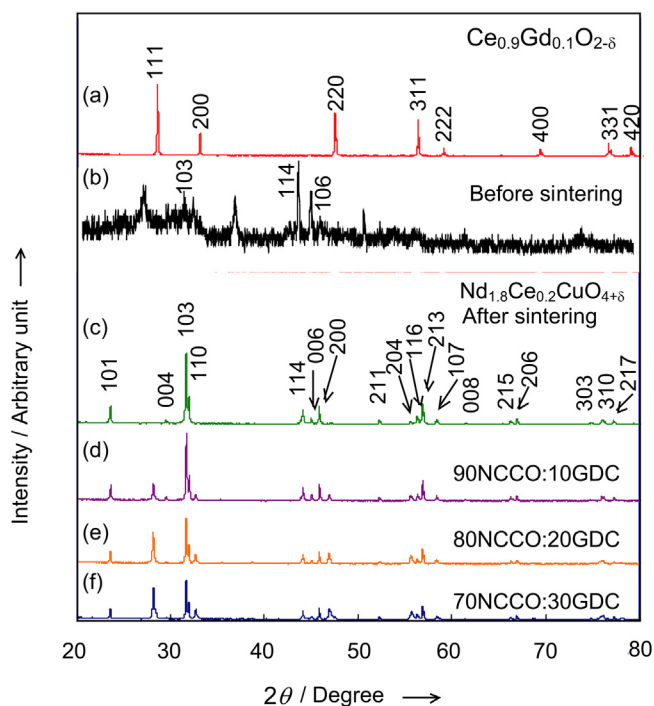

Fig. 2. The X-ray powder diffraction patterns of (a) CGO, (b) NCCO before sintering, (c) NCCO after sintering, (d) 90NCCO:10CGO, (e) 80NCCO:20CGO and (f) 70NCCO:30CGO.

Table 1
Comparison of relative vol.% of CGO (estimated from XRD data), lattice cell constants of NCCO and CGO, crystallite sizes of NCCO ($C_{s(NCCO)}$) and CGO ($C_{s(CGO)}$), relative density (ρ) and effective particle size <D> for (100 − x)NCCO:(x)CGO (x = 0–30 vol.%) composite system.

x (vol.%)	$x_{rel.}$ (vol.%)	a_{NCCO} (nm)	c_{NCCO} (nm)	a_{CGO} (nm)	$C_{s(NCCO)}$ (nm)	$C_{s(CGO)}$ (nm)	ρ (%)	<D> (nm)
0	0	0.394 ± 0.002	1.207 ± 0.002	–	273 ± 2	–	–	723 ± 76
10	08.9 ± 0.7	0.394 ± 0.003	1.205 ± 0.003	0.549 ± 0.004	258 ± 3	47 ± 2	95 ± 5	672 ± 52
20	21.2 ± 0.4	0.395 ± 0.005	1.206 ± 0.004	0.548 ± 0.005	236 ± 4	78 ± 1	96 ± 2	561 ± 21
30	29.7 ± 0.3	0.394 ± 0.003	1.208 ± 0.003	0.549 ± 0.003	193 ± 2	146 ± 3	95 ± 3	650 ± 43

obvious (Fig. 4(d)). No cracks and/or separation between electrode and electrolyte were observed after four heating and cooling cycles.

The particle size distribution of the 80NCCO:20CGO cathode in the prepared ink (four batches) is shown in Fig. 5. Apparently, the particle sizes and distribution are nearly same for all batches, indicating that the results are highly reproducible. The narrow distribution with an effective particle size ≈561 ± 21 nm (Table 1) is advantageous when producing good/stable ink.

3.3. d.c. conductivity

The variations in the d.c. conductivity as a parametric function of the temperature for 90NCCO:10CGO, 80NCCO:20CGO and 70NCCO:30CGO is depicted in Fig. 6. In the MIECs and composites, both the ions and electrons contribute to the total electrical conductivity. Because the electronic conductivity is usually much higher than the ionic conductivity, the total measured d.c. conductivity is primarily attributed to the electronic conductivity. The semiconductor to pseudo-metal phase transition (Fig. 6) in the temperature range 600–650 °C is observed in the pure NCCO and the 90NCCO:10CGO. A similar transition for the NCCO has been observed previously [8]. This transition, however, is not observed (within the temperature range of measurements) for the 80NCCO:20CGO and 70NCCO:30CGO composites. The absence of the semiconductor to pseudo-metal phase transition in these composites is attributed to the surface-activated superfine crystallites of NCCO. The suppression of the temperature-dependent transition due to nano-crystalline material is reported for the NCCO [13] and La$_{0.8}$Sr$_{0.2}$MnO$_3$ (LSM) [14]. All of the studied samples obey the Arrhenius law (Eq. (1)) below the transition temperature.

$$\sigma T = (\sigma T)_0 \exp\left(\frac{-E_a}{kT}\right), \tag{1}$$

where $(\sigma T)_0$, k, T and E_a are the pre-exponential factor, Boltzmann constant, absolute temperature and activation energy, respectively.

Further, the $\sigma(E_a)$ decreases (increases) when increasing the CGO concentration in the composites. Because increasing the number of electronically insulating CGO electrolyte grains hinder the electron/hole mobility/transport through the composites, the overall d.c. conductivity decreases when increasing the CGO content in the composite cathode. According to the literature, adding CGO increases the ionic conductivity while decreasing the overall conductivity of the composite cathodes [15].

3.4. Electrochemical impedance spectroscopy (EIS)

The typical complex impedance plots for Cell-82 at various temperatures are shown in Fig. 7(a). The exploded view of the complex impedance plot at 640 °C (Fig. 7(b)) consists of more than one semicircle. A similar trend in the temperature range of measurements was observed in the complex impedance plots for the studied cells. The impedance response suggests that the overall electrode reaction involves several processes, which occur simultaneously at different time scales, contributed significantly to R_p. The entire frequency response, however, could be deconvoluted to reveal the combination of at least a mid-frequency (MF) depressed semicircle and a low-frequency (LF) skewed semicircular arc (Fig. 7(b)). The absence of high frequency (HF) semicircle attributed to migration of O^{2-} through CGO electrolyte is due to limitations in the available frequency (≤1 MHz) [10]. The complex impedance data were analyzed in detail while using the software developed by Scribner advanced software for electrochemical research and development [16]. According to the literature, fewer circuits were considered while the most accurate fit for the measured impedance data was obtained. In addition, models were selected with individual circuits that represent single electrode processes, while the entire circuit model corresponds to the total electrode kinetics. Customarily, the complex impedance response of symmetric cell is modeled using a series resistor (R_s) in series with either two circuits that comprise a parallel combination of R and a constant phase element (CPE) or
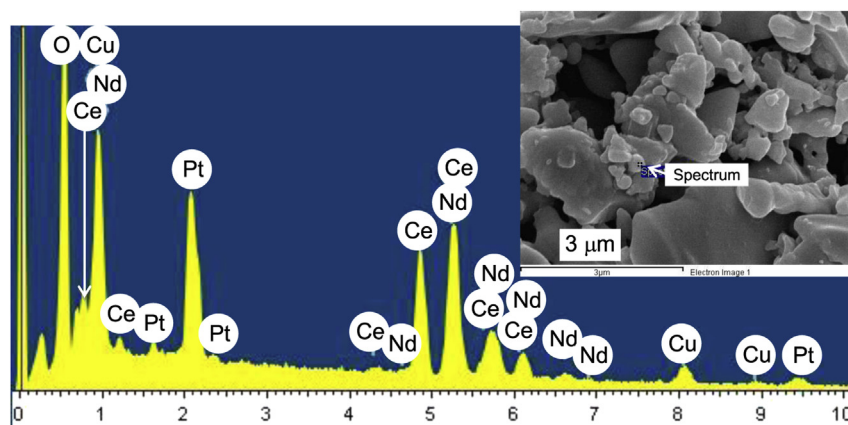
Fig. 3. EDS spectrum due to NCCO grain of 80NCCO:20CGO composite (Cell-82).

Table 2
A comparison of experimentally and theoretically estimated at.% of elements for $Nd_{1.8}Ce_{0.2}CuO_{4+\delta}$.

Element	at.%	
	Experimental	Theoretical
O	56.78	57.14
Cu	14.34	14.28
Ce	1.49	1.52
Nd	27.39	27.06

one parallel combination of R and CPE with one Gerischer element (GE). The continuous line in Fig. 7(b) represents the best complex non-linear least squares fit (least deviations) for the measured data (open circles) based on the proposed electrical equivalent circuit model (R_s–(R_1–CPE)–G) (inset of Fig. 7(b)). The dotted red lines in Fig. 7(b) visualize the individual electrical equivalent elements of the model that form the measured complex impedance spectrum. A similar R_s–(R_1–CPE)–G model is proposed for a $Ce_{0.8}Gd_{0.2}O_{1.95}$-impregnated $La_{0.99}Co_{0.4}Ni_{0.6}O_{3-\delta}$ composite cathode [17]. The resistance R_s of ECM is attributed to the migration of oxygen ions through the CGO electrolyte [10,11]. The MF arc is modeled using a parallel combination of R_1 and CPE. The literature suggests that the MF semicircle might be assigned to the polarization during the O^{2-} charge transfer across the gas/electrode/electrolyte interface (TPB) [17–19]. However, the LF impedance data (skewed semicircular arc) is accurately modeled using the Gerischer element (GE) (Fig. 7(b)).

According to Adler [20], two of the major kinetic processes of the oxygen electrode, which are the oxygen exchange and the oxide ion diffusion, can be coupled to form a single Gerischer impedance (Z_G) response. The general Z_G is expressed in Eq. (2),

$$Z_G = \frac{1}{Y_0\sqrt{K_A + i\omega}} = \frac{R_G}{\sqrt{1 + i\omega R_G C_G}}, \tag{2}$$

where Y_0 and K_A are the admittance and the rate constant, respectively. The Gerischer impedance response is applied to both the MIEC electrodes [21–23] and the three apparent phase boundaries of electrodes such as Pt/YSZ [24,25] and LSM/YSZ [26]. This value is also applied to the porous ceramic anode in SOFC [27]. The GE includes the ion transfer resistance (R_i), the electron transport resistance (R_e) so $R_2 = R_i + R_e$ and a CPE instead of an ideal capacitor. The ideal high frequency 45° slope of the Gerischer response reflects the electrochemical extension from the cathode/electrolyte interface out into the porous electrode [20,27]. The Gerischer response indicates that the diffusion of O^{2-} is one of the important steps in the overall ORR relatively high frequencies ($\approx 45°$ line in a Nyquist plot (Fig. 7(b)). A detailed theoretical description of Gerischer impedance is provided in the literature [20,23,28–30].

The zero-bias impedance (Z) of a symmetrical cell based on the ALS model (Adler–Lane–Steele) can be described using Eq. (3) [21,24]:

$$Z = R_{electrolyte} + Z_{interface} + Z_{chem} \tag{3}$$

where $Z_{electrolyte}$ is the electrolyte resistance; $Z_{interface}$ is the impedance attributed to both electron and ion transfer at the current collector/electrode and electrode/electrolyte interfaces. The Z_{chem} is the impedance attributed to the non-charge transfer process contributed by oxygen surface exchange, solid-state diffusion, and gas-phase diffusion inside and outside of the electrode. The ECM fitting results for all cells at various temperatures are compared in Table 3. R_1 is smaller than R_2 within the temperature
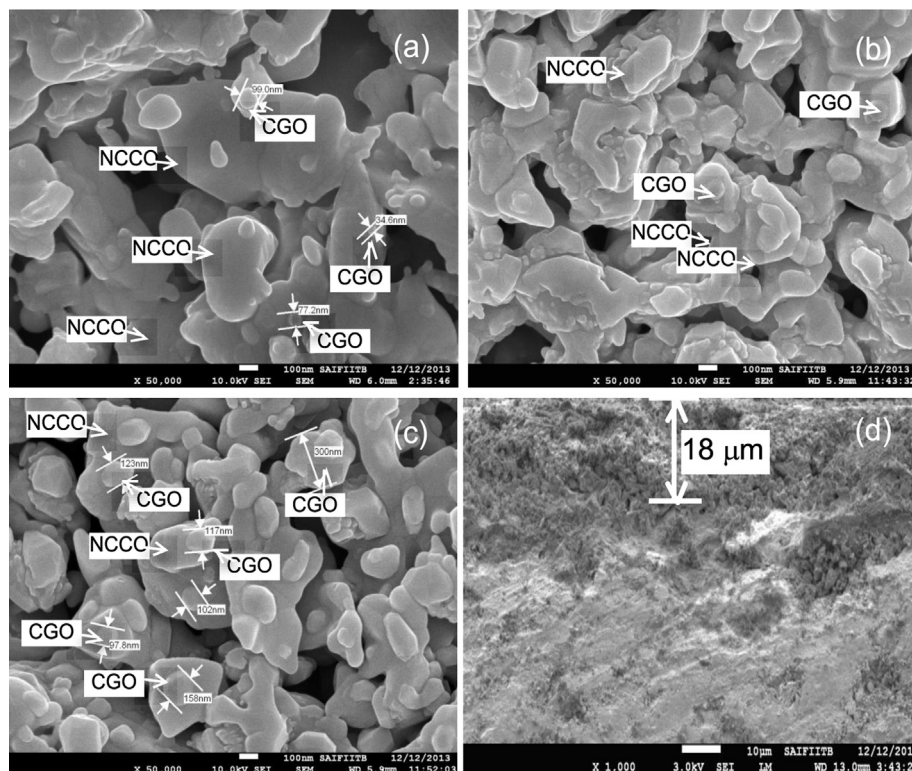

Fig. 4. Scanning electron microphotographs of cathode surface of (a) Cell-91, (b) Cell-82, (c) Cell-73 and (d) electrode/electrolyte interface of Cell-82.
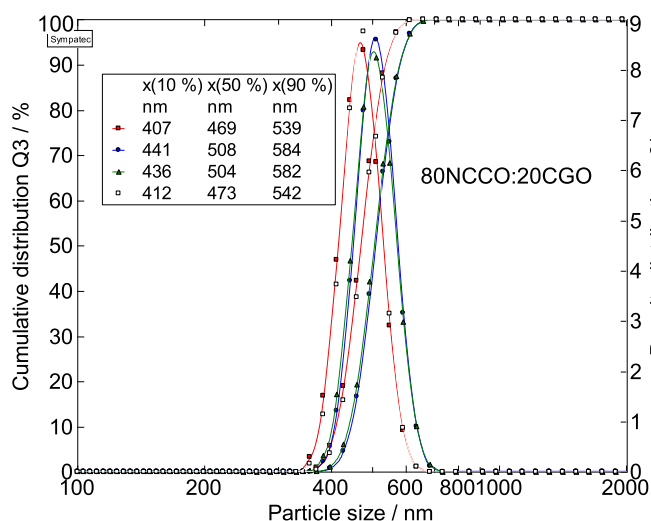
Fig. 5. Particle size distribution of 80NCCO:20CGO in the prepared ink/slurry (four batches).

range used when measuring the symmetric cells. Further, compared to the NCCO electrode, adding GDC to NCCO electrode reduces significantly the values of R_1 and R_2 at a fixed temperature, while the magnitude of CPE (CPE$-T_1$ and $G-T$) remains the same (Table 3). The temperature dependence of the HF resistance (R_s), the MF resistance (R_1) and the LF resistance, i.e., the GE response (R_2) of Cell-82, is presented in Fig. 8. Evidently, R_s, the R_1 and the R_2 exhibit Arrhenius behavior within the studied temperature range. The magnitude of the activation energy (E_a) 0.83 $\pm$ 0.005 eV, which is obtained from temperature-dependent R_s, is slightly lower than the lowest reported values for CGO ($E_a \approx$ 0.87–1.03 eV) [22,29–34]. The slightly lower value for the estimated E_a is attributed to the nano-sized CGO particles. Therefore, assuming that $R_{electrolyte} = R_s$ due to migration of O^{2-} through CGO electrolyte is justified. In addition, the decreased dependence of R_1 on the temperature (Fig. 8) agrees with previous reports [17]. The estimated magnitudes of the capacitances (Table 3) corresponding to the MF Z_{R_1-CPE} (C_{R_1-CPE}) and LF Z_G responses (C_G) are approximately 1×10^{-3} F cm^{-2} and 30×10^{-1} F cm^{-2}, respectively. The capacitance

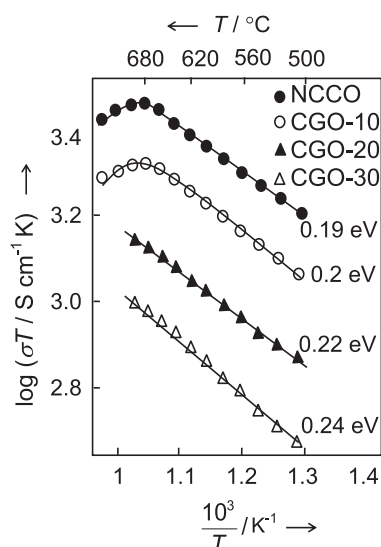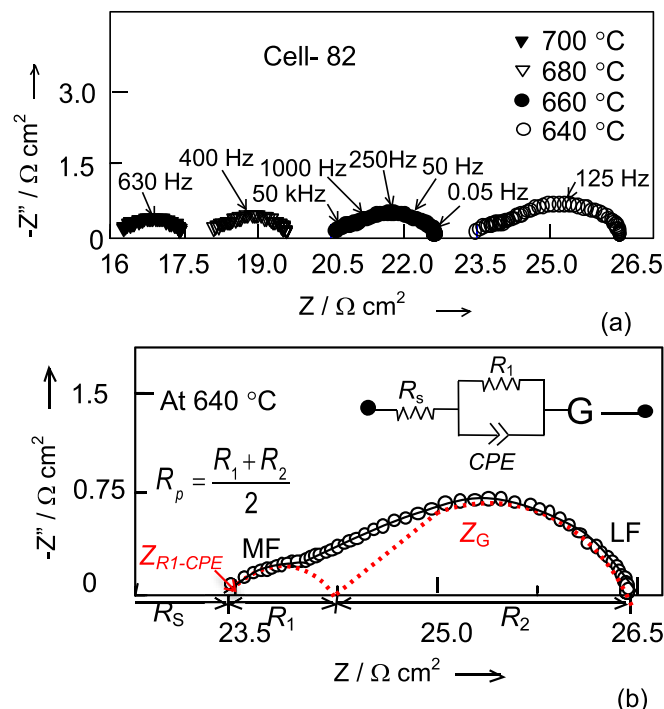Fig. 6. Arrhenius plots for $(100 - x)$NCCO:(x)CGO ($x = 0$–30) composite cathodes.

Fig. 7. Complex impedance plots for (a) Cell-82 at various temperatures and (b) experimental data (points) at 640 °C, simulated data (line), electrical equivalent circuit model and the response due to model used in the treatment of all the data for Cell-82 (For interpretation of the references to color in this figure legend, the reader is referred to the web version of the article).

values on the order of 10^{-3} F (Table 3) correspond to the MF arcs, which are comparable to the values reported for the cathodes [35–40]. Therefore the MF arc originates from the charge transfer reaction at the electrode/electrolyte interface [41,42]. The literature related to LSM−YSZ cathodes suggests that the ionic charge transfer from the electrode to electrolyte contributes to the total resistance of the cathode [43]. According to numerous researchers, the GE response occurs due to an electrochemical reaction coupled with O^{2-} diffusion [28–30]. The diffusion of O^{2-}, however, can occur through the bulk, along the surface or a combination of both. For the NCCO cathode, which is MIEC, the O^{2-} diffuses primarily through the bulk. These processes cause the relatively high capacitance values, which may range upward to 1 F cm^{-2} [24]. A comparable value relative to the C_G of 80NCCO−20CGO in the present composite cathode is observed (Table 3). The $Z_G = Z_{chem}$ is attributed to a non-charge-transfer process during the ORR. Similarly, the low-frequency semicircle is ascribed to non-charge transfer processes, such as oxygen surface exchange and gas-phase diffusion through the porous cathode layer, in the literature [44–47]. Mitterdorfer et al. [48] reported a GE-like impedance response for the LSM−YSZ composite cathode with a capacitance value of approximately 100×10^{-6} F cm^{-2}. According to the literature, these data suggest that the ionic transport is confined to the surface rather than the bulk [17]. The transfer of O^{2-} across the electrode/electrolyte interface should occur within a narrow depth close to the TPB for the cathode, while the oxide ion diffusion is confined to the surface [17]. In contrast, a much larger fraction of the electrode/electrolyte interface is active during the O^{2-} charge transfer in case of MIEC electrode. The capacitance of this reaction step should be similar to the MF Z_{R_1-CPE} response (C_{R_1-CPE}). The MF Z_{R_1-CPE} response should be due to the O^{2-} transfer at the electrode/electrolyte interface for the 80NCCO−20CGO composite. Similarly,

Table 3
Comparison of fitted electrical circuit element series resistance (R_s), resistance/capacitance due to MF response (R_1/CPE−T_1), resistance/capacitance due to LF response (R_2/G−T) values corresponding to EIS data of Cell-00, Cell-91 and Cell-82 and Cell-73 at various temperatures.

Sr. No	T (°C)	R_s (Ω cm²)	R_1 (Ω cm²)	R_2 (Ω cm²)	CPE−T_1 (mF cm⁻²)	CPE−P_1	G−T (F cm⁻²)	G−P
Cell-00								
1	700	2.96 ± 0.3	0.29 ± 0.2	1.20 ± 0.4	1.79 ± 0.04	0.48 ± 0.001	0.97 ± 0.003	0.42 ± 0.004
2	660	7.07 ± 0.1	1.42 ± 0.1	1.16 ± 0.2	2.17 ± 0.05	0.57 ± 0.002	0.91 ± 0.007	0.34 ± 0.005
3	640	11.76 ± 0.3	1.82 ± 0.3	2.27 ± 0.3	1.78 ± 0.02	0.49 ± 0.004	0.84 ± 0.005	0.29 ± 0.002
4	600	30.32 ± 0.2	2.95 ± 0.1	5.07 ± 0.1	0.45 ± 0.07	0.52 ± 0.010	0.56 ± 0.007	0.21 ± 0.003
Cell-91								
7	700	3.08 ± 0.1	0.098 ± 0.007	0.358 ± 0.003	2.15 ± 0.05	0.99 ± 0.002	1.14 ± 0.002	0.78 ± 0.002
9	660	6.18 ± 0.4	0.920 ± 0.005	0.822 ± 0.005	2.09 ± 0.02	0.86 ± 0.007	0.92 ± 0.003	0.75 ± 0.006
10	640	11.15 ± 0.3	1.468 ± 0.005	1.321 ± 0.003	1.57 ± 0.05	0.83 ± 0.002	0.73 ± 0.002	0.72 ± 0.002
12	600	33.64 ± 0.3	1.972 ± 0.004	3.154 ± 0.003	1.12 ± 0.04	0.81 ± 0.005	0.53 ± 0.004	0.69 ± 0.003
Cell-82								
7	700	3.02 ± 0.3	0.079 ± 0.002	1.097 ± 0.004	2.43 ± 0.03	1.14 ± 0.007	1.29 ± 0.005	0.89 ± 0.002
9	660	7.31 ± 0.3	0.089 ± 0.005	1.402 ± 0.003	2.14 ± 0.04	0.97 ± 0.005	0.97 ± 0.006	0.81 ± 0.004
10	640	11.27 ± 0.5	0.979 ± 0.004	1.656 ± 0.005	2.09 ± 0.02	0.91 ± 0.003	0.84 ± 0.002	0.79 ± 0.003
12	600	33.71 ± 0.2	1.086 ± 0.002	2.203 ± 0.004	1.78 ± 0.03	0.89 ± 0.003	0.66 ± 0.004	0.72 ± 0.007
Cell-73								
7	700	3.18 ± 0.4	0.099 ± 0.004	0.475 ± 0.007	2.33 ± 0.04	0.75 ± 0.002	1.02 ± 0.007	0.67 ± 0.003
9	660	7.70 ± 0.3	0.982 ± 0.003	1.023 ± 0.002	1.87 ± 0.05	0.79 ± 0.003	0.95 ± 0.004	0.68 ± 0.004
10	640	12.05 ± 0.3	1.687 ± 0.003	1.912 ± 0.007	1.38 ± 0.04	0.84 ± 0.004	0.68 ± 0.003	0.66 ± 0.002
12	600	34.17 ± 0.4	2.213 ± 0.002	4.487 ± 0.005	1.06 ± 0.02	0.86 ± 0.003	0.47 ± 0.004	0.65 ± 0.004

the MF and LF responses are correlated with the ion and electron (charge) transfers at the electrode/electrolyte, the collector/electrode interfaces and the non-charge transfers, such as oxygen surface exchange and gas-phase diffusion inside and outside the electrode layer, respectively [41]. The reduction in both the R_1 (MF) and the R_2 (LF) values (Table 3) indicate that the ORR process improves after impregnating the NCCO with nano-crystalline CGO. In addition, having a higher R_2 than R_1 implies that the non-charge-transfer reaction is the major ORR rate-limiting step for the composite cathode. Adler [49] suggested that the non-charge-transfer process might be a rate-determining step during ORR. Furthermore, the ORR process might be determined by the concentration and the chemical potential gradients that occur over macroscopic distances when nearly 100% electrode surface and bulk electrolyte are involved.

The total electrode polarization resistance (R_p) at each temperature for all symmetric cells was estimated from the magnitudes of R_1 and R_2 obtained from Nyquist plots using Eq. (4):
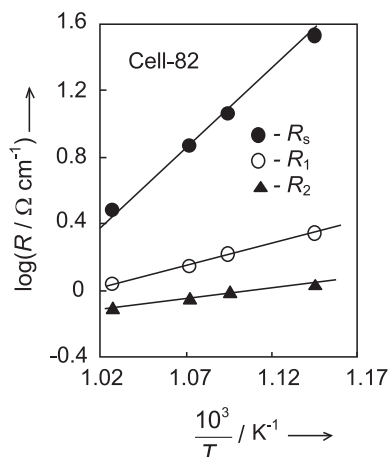
$$R_p = \frac{R_1 + R_2}{2} \tag{4}$$

The temperature-dependent R_p are compared in Fig. 9, revealing the lowest R_p value (0.23 ± 0.07 Ω cm² at 700 °C) and activation energy ($E_a = 0.88 \pm 0.03$ eV) across the entire temperature range for the Cell-82 measurements compared to the other studied cells (Cell-91, Cell-82, Cell-73 and Cell-00). The E_a values for Cell-91, Cell-82, Cell-73 and Cell-00 are 0.93, 0.88, 0.92 and 1.4 eV, respectively; these values fall within the range for MIECs. The decrease in activation energy after CGO impregnation suggests that the ORR reaction mechanism changes. Hjalmarsson and Mogensen [17] reported almost no change in E_a after CGO infiltration in a La$_{0.99}$Co$_{0.6}$Ni$_{0.4}$O$_3$ cathode. Similarly, no change in reaction mechanism is suggested for the LSM−CGO [50] and Ca$_2$Fe$_{1.4}$Co$_{0.6}$O$_5$−CGO [51] composites. Nonetheless, a significantly lower E_a value for the oxygen ion conductor dispersed composite is reported for SmBaCoFeO$_{5-\delta}$−60CGO [52], LaSrCoFeO−36CGO [53], LaSrCoFeO−CGO [54,55], and Sm$_{1.8}$Ce$_{0.2}$CuO$_4$−CGO [37] compared to pure MIECs; the authors attributed this pattern to a change in the reaction mechanism. Because NCCO with K$_2$NiF$_4$-type structure is MIEC, the ORR occurs not only at the TPB layer but also throughout the entire

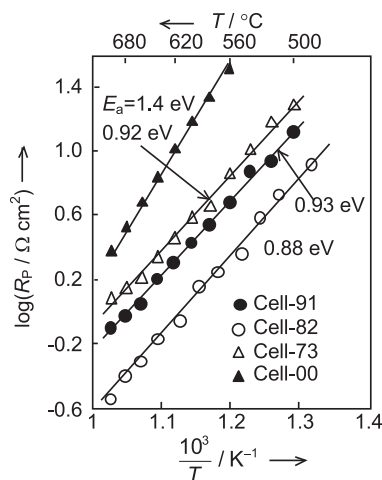**Fig. 8.** Arrhenius plots of R_s, R_1 and R_2 of Cell-82.

Fig. 9. Arrhenius plots for polarization resistance (R_p) of Cell-00, Cell-91, Cell-82 and Cell-73.

electrode. The initially adsorbed O_2 is reduced to O^{2-} after dissociation. Later, the O^{2-} is transferred across the electrode/electrolyte interface and the bulk electrolyte. The O^{2-} transfer rate is governed by the concentration of the oxygen vacancies in the NCCO. The O^{2-} transfer ability improves after nanocrystalline O^{2-} conducting CGO is impregnated in the superfine NCCO matrix because the electrochemical ORR reaction zone becomes enlarged. Additionally, the adhesion between the electrode and electrolyte improves significantly after impregnating NCCO with CGO, decreasing the electrode-electrolyte interface resistance that is pertinent to O^{2-} transfer. Both of these factors enhance the overall electrochemical performance (reduced R_p and E_a) of oxygen ion conducting, CGO-impregnated NCCO composite cathode.

The minimum R_p and E_a values for the 80NCCO:20CGO cathode can be understood based on the effective medium percolation theory [53,56]. In addition, the increased ionic conductivity attributed to the impregnation of CGO in NCCO reduces the effective charge transfer resistance (R_{ct}^{eff}) of the composite cathode according to the simplified Tanner Eq. (5) [57]:

$$R_{ct}^{eff} \approx \sqrt{\frac{BR_{ct}}{\sigma_i(1-V_v)}} \tag{5}$$

where B, R_{ct}, σ_i and V_v are the grain size of the CGO electrolyte in the composite electrode, the intrinsic charge transfer resistance (for pure electronic conducting cathode), the ionic conductivity of the electrolyte (different than the dense electrolyte) and the fractional porosity, respectively. The uniform and optimum porosity for 80NCCO:20CGO cathode are obtained (Fig. 4(b)) due to smallest effective particle size ($<D> = 561 \pm 21$ nm) along with their narrowest distribution compared to other (Table 1). The R_{ct}^{eff} is, thus, minimum for 80NCCO:20CGO cathode. According to Martinez and Brouwer [56] the TPBs are characterized by the adjacency and electrochemical interaction of electron conducting, ion conducting and gaseous specie. In addition, percolation of the ionic and electronic phases to the bulk electron and ion conductors at either end of the interface is required to make a TPB electrochemically active. High volumetric density of TPBs is achieved in Cell-20 due to the optimum volumetric fractions of both the NSNO and the CGO along with the maximum fractional porosity achieved through microstructure (Fig. 4(b)). Dusastre and Kilner [53] and Murray et al. [54], also, reported that the ambipolar transport behavior of composite

mixed ionic-electronic conductors is a function of the volume fraction of each of the randomly distributed constituent phases. Further, the optimum performance of cathode is correlated with percolation threshold. The high performance of 80NCCO:20CGO composite electrodes is consistent with the effective medium percolation theory. The overall performance of a porous electrode is, thus, not only determined by the mixed conducting transport properties in the solid phase of the electrode, but also by the inherent catalytic property of the TPB/2 PB and by the gas transport to, or away, from TPB/2 PB.

To understand the ORR mechanism, complex impedance measurements were carried out versus the oxygen partial pressure (P_{O_2}) at 550, 650 and 700 °C. The variations in $\log(R_1)$ and $\log(R_2)$ with the changes in $\log(P_{O_2})$ are shown in Fig. 10(a) and (b), respectively. Both R_1 and the R_2 are decreased significantly due to the increased oxygen partial pressure, as represented by Eq. (6):

$$R = R^0(P_{O_2})^{-n} \tag{6}$$

According to the literature, information regarding the rate-limiting step of the ORR at the electrode can be obtained from the n-values [26].

$$n = 1, \quad O_2(g) \Leftrightarrow O_{2,abs} \tag{7}$$

$$n = \frac{1}{2}, \quad O_{2,abs} \Leftrightarrow 2O_{abs} \tag{8}$$

$$n = \frac{3}{8}, \quad O_{TPB} + e' \Leftrightarrow O_{TPB}^- \tag{9}$$

$$n = \frac{1}{4}, \quad O_{abs} + 2e' + V_O^{\bullet\bullet} \Leftrightarrow O_O^x \tag{10}$$

$$n = \frac{1}{8}, \quad O_{TPB}^- + e' \Leftrightarrow O_{TPB}^{2-} \tag{11}$$

$$n = \frac{1}{10}, \quad O_{TPB}^{2-} + V_O^{\bullet\bullet} \Leftrightarrow O_O^x \tag{12}$$

Researchers have offered a few different sub-reactions for the same overall ORR [20,58]. The adsorbed oxygen atoms, O^- and O^{2-} can appear during one or more steps. Generally, the TPB region
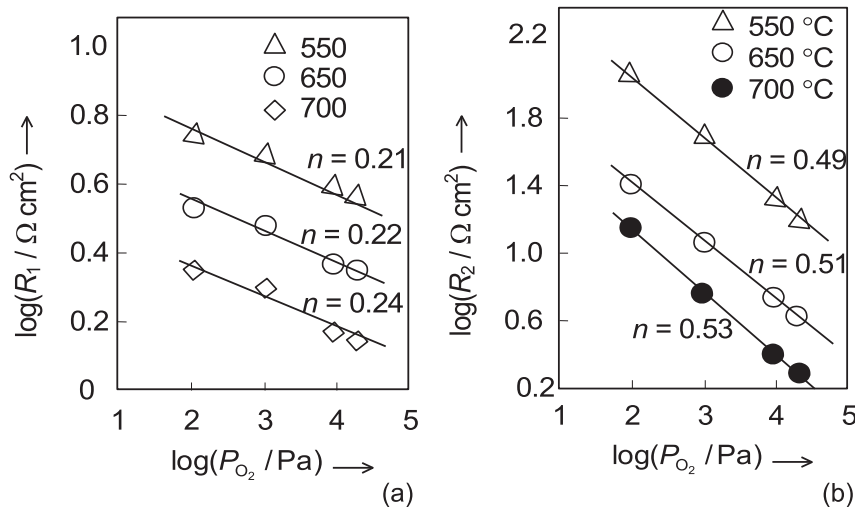

Fig. 10. Variation of polarization resistance (R_p) with oxygen partial pressure for Cell-82 estimated from (a) mid-frequency (MF) and (b) low-frequency (LF) impedance responses at 550, 650 and 700 °C.

where the cathode, electrolyte and gas make contact should be the key reaction region for the LSM/YSZ composites. The K_2NiF_4-type NCCO cathode material, however, is a mixed ionic and electronic conductor; therefore, the ORR also occurs at the gas/cathode interfaces, which are the two-phase boundary (2 PB) regions. Therefore, two charge transfer pathways co-exist and compete under different operating conditions. In addition to the reduction of oxygen, the diffusion of O^{2-} is the other important step for the cathode reaction process in this case. One or more of the above-mentioned ORR steps (Eqs. (7)–(12)) might be rate limiting. The relatively slow changes in R_1 versus R_2 for the measured ranges of the oxygen partial pressure and temperature are evident when comparing Fig. 10(a) and (b). Additionally, the polarization resistance pertinent to the LF arc (R_2) is generally larger than that related to the MF arc (R_1). A magnitude of n near 0.25 suggests that the R_1 is related to the charge-transfer reaction process (Eq. (10)). The $n \approx 0.5$ corresponding to the LF response polarization resistance R_2 suggests that the dissociative adsorbed oxygen diffuses on the cathode surface (Eq. (8)). These results substantiate the interpretation of the complex impedance results discussed above: the MF and LF responses are attributed to a charge transfer step and the non-charge transfer oxygen adsorption–desorption along with the diffusion during ORR, respectively. Similar rate-limiting steps are proposed for $La_{1.6}Sr_{0.4}NiO_4$:Ag [59] and $Sm_{1.8}Ce_{0.2}CuO_4$:-$Ce_{0.9}Gd_{0.1}O_{1.95}$ [37] composite cathodes. Interestingly, $n = 0.1$ (Eq. (11)) for the LSM/YSZ composite cathode due to the oxygen ion transfer from the triple phase boundary (TPB) to the electrolyte [46]. Comparing the results in Fig. 10(a) and (b) reveals that the non-charge transfer oxygen adsorption–desorption process is the major rate limiting step for the studied composite cathodes across the studied oxygen partial pressure and temperature ranges.

The R_p of the optimized composition are compared to the literature data for K_2NiF_4-type MIEC:oxyion conducting electrolyte composite cathodes in Table 4 [18,37,61–64]. A close examination of the table indicates that both the optimized composition (80NCCO:20CGO) and the $R_p = 0.23$ Ω cm^2 at 700 °C in present study are significantly different from the previously optimized composition (70NCCO:30CGO) and $R_p = 0.3$ Ω cm^2 at 700 °C [64]. These differences in the compositions and R_p values are attributed to the changes in the dispersion technique for CGO in NCCO. Commercial nano-crystalline CGO is dispersed as received in the NCCO matrix via ball-milling in an earlier study [64]. The smaller CGO crystallites (47–87 nm) in present study relative to previous studies (107–138 nm) improve the ORR sites while allowing facile O^{2-} diffusion and generating better interface contacts. Numerous studies reported the optimization of the electrolyte (second phase) in the cathode [53,65–67]. Adding 50 wt.% CGO to

a $La_{0.6}Sr_{0.4}Co_{0.2}Fe_{0.8}O_{3-\delta}$ (LSCF) cathode decreased R_p at low temperatures compared to a cathode containing 30 wt.% CGO [65]. A mixture of 40 vol.% LSGM in LSCF exhibited low R_p [65]. R_p is optimized for $La_{0.6}Sr_{0.4}Co_{0.2}Fe_{0.8}O_{3-\delta}$:(36 vol.%) $Ce_{0.9}Gd_{0.1}O_{2-\delta}$ [53], $La_{0.6}Sr_{0.4}Co_{0.2}Fe_{0.8}O_{3-\delta}$:(60 wt.%)$Ce_{0.9}Gd_{0.1}O_{2-\delta}$ [55], $LaBa_{0.5}Sr_{0.5}Co_2O_{5+\delta}$:(40 wt.%)$Ce_{0.9}Gd_{0.1}O_{2-\delta}$ [68], $La_{1-x}Sr_xMnO_3$:(40 wt.%)YSZ [60] and $Sm_{1.8}Ce_{0.2}CuO_4$:(06 vol.%) $Ce_{0.9}Gd_{0.1}O_{1.95}$ [60], $Pr_{0.58}Sr_{0.4}Fe_{0.8}Co_{0.2}O_{3-\delta}$:(50 wt.%) $Ce_{0.9}Gd_{0.1}O_{1.95}$ [15], (La,Sr) (Co,Fe)O$_3$:(50 vol.%)(Ce,Gd)O$_3$ [54]. The 80NCCO:20CGO composite exhibits competitive R_p values when compared to K_2NiF_4-type composite cathodes (Table 4).

4. Conclusions

The impregnation of a stoichiometric solution of cerium and gadolinium nitrates followed by sintering at 900 °C for 4 h disperses nano-crystalline oxy-ion-conducting $Ce_{0.9}Gd_{0.1}O_{2-\delta}$ electrolyte in a superfine crystalline $Nd_{1.8}Ce_{0.2}CuO_{4+\delta}$, generating a mixed ionic-electronic conductor. Although adding $Ce_{0.9}Gd_{0.1}O_{2-\delta}$ to the $Nd_{1.8}Ce_{0.2}CuO_{4+\delta}$ matrix reduces the electronic conductivity, the effective oxygen reduction reaction zone is enlarged, which significantly reduces the electrode polarization resistance (R_p) of the composite cathode. The minimum values for both the R_p (0.23 $\pm$ 0.02 Ω cm^2 at a temperature of 700 °C) and the E_a (0.88 $\pm$ 0.03 eV) for (80)$Nd_{1.8}Ce_{0.2}CuO_{4+\delta}$:(20)$Ce_{0.9}Gd_{0.1}O_{2-\delta}$ are due to the optimally dispersed $Ce_{0.9}Gd_{0.1}O_{2-\delta}$ in the porous $Nd_{1.8}Ce_{0.2}CuO_{4+\delta}$ matrix. The $Ce_{0.9}Gd_{0.1}O_{2-\delta}$ dispersed via impregnation is superior to the composite obtained via ball-milling. The successfully modeled impedance spectra with an electrical equivalent consisting of a mid-frequency Z_{R_1-CPE} circuit in series with a low-frequency Gerischer impedance (Z_G) suggests that diffusion and the charge transfer and the non-charge transfer oxygen adsorption-desorption are the major rate limiting steps during the oxygen reduction reaction process. Impregnating $Nd_{1.8}Ce_{0.2}CuO_{4+\delta}$ with $Ce_{0.9}Gd_{0.1}O_{2-\delta}$ may generate a composite cathode with an improved electrochemical performance.

Table 4
A comparison of polarization resistance (R_p) obtained in this study with reported in the literature for (K_2NiF_4):(oxy-ion conductor) composite cathodes.

Sr.#	Cathode	R_p (Ω cm^2)	T (°C)	Ref.
1	80$Pr_{1.6}Sr_{0.4}NiO_4$:20 (wt.%)YSZ	0.23	750	Huang et al. [61]
2	94$Sm_{1.8}Ce_{0.2}CuO_4$:06 (vol.%)$Ce_{0.9}Gd_{0.1}O_{1.95}$	0.17	750	Sun et al. [37]
3	70$La_{1.6}Sr_{0.4}NiO_{4+\delta}$:30 (wt.%)$Ce_{0.8}Sm_{0.2}O_{1.9}$	0.425	750	Gong et al. [62]
4	70$Ba_{1.2}Sr_{0.8}CoO_{4+\delta}$:30 (wt.%)$Ce_{0.9}Gd_{0.1}O_{1.9}$	0.17	750	Jin and Liu [63]
5	$La_{0.99}Co_{0.4}Ni_{0.6}O_3$: $Ce_{0.9}Gd_{0.1}O_{1.9}$	0.18	750	Henuveln et al. [18]
6	70$Nd_{1.8}Ce_{0.2}CuO_{4+\delta}$:30 (vol.%)$Ce_{0.9}Gd_{0.1}O_{2-\delta}$	0.34	700	Khandale et al. [64]
7	20$Nd_{1.8}Ce_{0.2}CuO_{4+\delta}$:20 (vol.%)$Ce_{0.9}Gd_{0.1}O_{2-\delta}$	0.23	700	Present study

References

[1] Z. Liu, D. Ding, B. Liu, W. Guo, W. Wang, C. Xia, J. Power Sources 196 (2011) 8561–8567.
[2] S.P. Jiang, Y.Y. Duan, J.G. Love, J. Electrochem. Soc. 149 (2002) A1175–A1183.
[3] S.P. Jiang, Y.J. Leng, S.H. Chan, K.A. Khor, Electrochem. Solid State Lett. 6 (2003) A67–A70.
[4] S.P. Jiang, S. Zhang, Y.D. Zhen, W. Wang, J. Am. Ceram. Soc. 88 (2005) 1779–1785.
[5] B. Huang, X.J. Zhu, Y. Lv, H. Liu, J. Power Sources 209 (2009) 209–219.
[6] Y. Wang, H. Zhang, F. Chen, C. Xi, J. Power Sources 203 (2012) 34–41.
[7] S. Huang, S. Feng, H. Wang, Y. Li, C. Wang, Int. J. Hydrogen Energy 36 (2011) l0968–l0974.
[8] A.P. Khandale, S.S. Bhoga, J. Solid State Electrochem. 16 (2012) 341–352.
[9] Q. Huang, R. Hui, B. Wang, J. Zhang, Electrochim. Acta 52 (2007) 8144–8164.
[10] A.P. Khandale, S.S. Bhoga, J. Alloys Compd. 509 (2011) 6955–6961.
[11] V.N. Chaudhari, A.P. Khandale, S.S. Bhoga, J. Power Sources 248 (2014) 647–654.
[12] Y.J. Leng, S.H. Chan, K.A. Khor, S.P. Jiang, Int. J. Hydrogen Energy 10 (2006) 339–347.
[13] A.P. Khandale, S.S. Bhoga, Electrochim. Acta 56 (2011) 9219–9223.
[14] K.R. Nagde, S.S. Bhoga, Ionics 16 (2010) 36–370.
[15] P.K. Patro, T. Delahaye, E. Bouyer, Solid State Ionics 181 (2010) 1378–1386.
[16] Scribner Associates. Inc., Southern Pines, NC, www.Scribner.com, 2003.
[17] P. Hjalmarsson, M. Mogensen, J. Power Sources 196 (2011) 7237–7244.
[18] F.H. Henuveln, H.J.M. Bouwmeester, J. Electrochem. Soc. 144 (1997) 134–137.

[19] Y.J. Leng, S.H. Chan, K.S. Khor, S.P. Jiang, Int. J. Hydrogen Energy 29 (2004) 1025–1033.
[20] S.B. Adler, Chem. Rev. 104 (2004) 4791–4843.
[21] S.B. Adler, Solid State Ionics 111 (1998) 125–134.
[22] A.P. Khandale, S.S. Bhoga, R.V. Kumar, Solid State Ionics 238 (2013) 1–6.
[23] J. Nielsen, P. Hjalmarsson, M.H. Hansen, P. Blennow, J. Power Sources 245 (2014) 418–428.
[24] S.B. Adler, J.A. Lane, B.C.H. Steele, J. Electrochem. Soc. 143 (1996) 3554–3564.
[25] A. Mitterdorfer, L.J. Gauckler, Solid State Ionics 117 (1999) 187–202.
[26] E. Siebert, A. Hammouche, M. Kleitz, Electrochim. Acta 40 (1995) 1741–1753.
[27] M. González-Cuenca, W. Zipprich, B.A. Boukamp, G. Pudmich, F. Tietz, Fuel Cells 1 (2001) 256–264.
[28] H. Gerischer, Z. Phys. Chem. 198 (1951) 286–313.
[29] B.A. Boukamp, H.J.M. Bouwmeester, Solid State Ionics 157 (2003) 29–33.
[30] B.A. Boukamp, Solid State Ionics 169 (2004) 65–73.
[31] K. Singh, S.A. Acharya, S.S. Bhoga, Ionics 12 (2006) 295–301.
[32] K. Muthukkumaran, P. Kuppusami, E. Mohandas, V.S. Raghunathan, S. Selladurai, in: International Symposium on Research Students Materials Science and Engineering, 2004, p. 1.
[33] S. Kuharuangrong, J. Power Sources 171 (2) (2007) 506–510.
[34] B.C.H. Steele, Solid State Ionics 129 (2000) 95–110.
[35] D.J. Chen, R. Ran, K. Zhang, J. Wang, Z.P. Shao, J. Power Sources 188 (2009) 96–105.
[36] T. Horita, K. Yamaji, N. Sakai, H. Yukokawa, A. Weber, E. Ivers-Tiffee, Electrochim. Acta 46 (2001) 1837–1845.
[37] L.P. Sun, H. Zhao, Q. Li, L.H. Huo, J.P. Viricelle, C. Pijolat, Int. J. Hydrogen Energy 36 (2011) 12555–12560.
[38] N.T. Hart, M.P. Brandon, M.J. Day, N. Lapena-Rey, J. Power Sources 106 (2002) 42–50.
[39] Y. Takeda, R. Kanno, M. Noda, Y. Tomida, O. Yamamoto, J. Electrochem. Soc. 134 (1987) 2656–2661.
[40] J. Fleig, F.S. Baumann, V. Brichzin, H.R. Kim, J. Jamnik, G. Cristiani, H.U. Habermeier, J. Maier, Fuel Cells 6 (2006) 284–292.
[41] S.B. Adler, X.Y. Chen, J.R. Wilson, J. Catal. 245 (2007) 91–109.
[42] C. Zhu, X. Liu, D. Xu, D. Wang, D. Yan, L. Pei, T. Lu, W. Su, J. Power Sources 185 (2008) 212–216.
[43] M. Mogensen, in: Proceedings of the 14th International Symposium on Materials Science, 1993, pp. 117–120.
[44] S. Pang, X. Jiang, X. Li, Q. Wang, Z. Su, Q. Zhang, Int. J. Hydrogen Energy 37 (2012) 3998–4001.
[45] Y. Hu, C. Bogicevic, Y. Bouffanais, M. Giot, O. Hernandez, G. Dezanneau, J. Power Sources 242 (2013) 50–56.
[46] X. Che, Y. Shen, H. Li, T. He, J. Power Sources 222 (2013) 288–293.
[47] F. Mauvy, C. Lalanne, J.M. Bassat, J.C. Grenier, H. Zhao, L. Huo, P. Stevens, J. Electrochem. Soc. 153 (2006) A1547–A1553.
[48] A. Mitterdorfer, L.J. Gauckler, Solid State Ionics 111 (1998) 185–218.
[49] S.B. Adler, Solid State Ionics 135 (2000) 603–612.
[50] Y.J. Leng, S.H. Chan, K.A. Khor, S.P. Jiang, J. Solid State Electrochem 10 (2006) 339–347.
[51] Q. Li, L.P. Sun, L. Huo, H. Zhao, J.C. Grenier, J. Solid State Electrochem 16 (2011) 1169–1174.
[52] S. Lu, G. Long, Y. Ji, X. Meng, C. Sun, Int. J. Hydrogen Energy 35 (2010) 7930–7935.
[53] V. Dusastre, J.A. Kilner, Solid State Ionics 126 (1999) 163–174.
[54] E.P. Murray, M.J. Sever, S.A. Barnett, Solid State Ionics 148 (2002) 27–34.
[55] Y. Leng, S.H. Chan, Q. Liu, J. Hydrogen Energy 33 (2008) 3808–3817.
[56] A.S. Martinez, J. Brouwer, Electrochim. Acta 53 (2008) 3597–3609.
[57] C.W. Tanner, K.Z. Fung, A.V. Virkar, J. Electrochem. Soc. 144 (1997) 21–30.
[58] Y. Li, R. Gemmen, X. Liu, J. Power Sources 195 (2010) 3345–3358.
[59] Q. Li, L.P. Sun, L.H. Huo, H. Zhao, J.C. Grenier, J. Power Sources 196 (2011) 1712–1716.
[60] J.D. Kim, G.D. Kim, J.W. Moon, Y. Park, W.H. Lee, K. Kobayashi, M. Nagai, C.E. Kim, Solid State Ionics 143 (2001) 379–389.
[61] X. Huang, F. Zhang, Z. Lu, B. Wei, T. Li, Z. Wang, W. Su, J. Phys. Chem. Solids 70 (2009) 665–668.
[62] M. Gong, L. Lu, H. Zhang, L. Gao, Y. Guo, J. Jin, Mater. Res. Bull. 44 (2009) 1630–1634.
[63] C. Jin, J. Liu, J. Alloys Compd. 474 (2009) 573–577.
[64] A.P. Khandale, S.S. Bhoga, Electrochim. Acta 130 (2014) 439–445.
[65] W.G. Wang, M. Mogensen, Solid State Ionics 176 (2005) 457–462.
[66] H. Gu, H. Chen, L. Gao, L. Guo, Electrochim. Acta 54 (2009) 7094–7098.
[67] B. Fan, X. Liu, Solid State Ionics 180 (2009) 973–977.
[68] S. Choi, S. Park, J. Kim, T.H. Lim, J. Shin, G. Kim, Electrochem. Commun. 34 (2013) 5–8.